Deformation Textures of AA8011 Aluminum Alloy Sheets Severely Deformed by Accumulative Roll Bonding

HYOUNG WOOK KIM, SUK BONG KANG, NOBUHIRO TSUJI, and YORITOSHI MINAMINO

A fully annealed AA8011 aluminum alloy sheet containing a number of large particles (~5 μm) was severely deformed up to an equivalent strain of 12 by an accumulative roll-bonding (ARB) process. The texture evolution during the ARB process was clarified, along with the microstructure. The ARB-processed aluminum alloy sheets had a different texture distribution through the sheet thickness, due to the high friction between the roll and the material during the ARB process. The shear textures composed of {001}<110> and {111}<110> orientations developed at the sheet surface, while the rolling textures, including Cu {112}<111> and Dillamore {4,4,11}<11,11,8> orientations, developed at the sheet center. The textural change from a shear texture to a rolling texture at the sheet center during the ARB process contributed to an increase in the fraction of high-angle boundaries. Also, a large number of second-phase particles in the AA8011 alloy sheets weakened the texture. Up to the medium strain range (below $\varepsilon = 6.4$), relatively weak textures developed, due to the inhomogeneous deformation around the second-phase particles; after the strain of 6.4, strong rolling-texture components, such as the Dillamore and Cu orientations, developed. This remarkable textural change can be explained by the reprecipitation of fine particles in grain interiors.

I. INTRODUCTION

RECENTLY, there have been developed various kinds of severe-plastic-deformation (SPD) processes, such as accumulative roll bonding (ARB), equal-channel angular pressing (ECAP), and high-pressure torsion (HPT).[1] It is well known that the SPD processes can fabricate a submicron/nanograin structure in various kinds of metals and alloys. Among these processes, the ARB process[1,2] is the most probable one to use in manufacturing large bulky ultrafine-grained (UFG) materials. The ARB process has been successfully applied to various kinds of metallic materials.[3–16] All these ARB-processed materials had microstructures composed of submicron grains, with a large misorientation angle and very high strength at ambient temperature. Detailed microstructural investigations showed that the grain refinement resulting from the ARB process could be achieved by grain subdivision and enhanced recovery, to form high-angle grain boundaries;[7,17–20] the microstructural evolution during the ARB process and subsequent annealing leads to the mechanism of continuous recrystallization (or *in-situ* recrystallization).[7,17–23] Some researchers[7,22,24] have recently reported the relationship between the mechanical properties and the microstructural features such as grain size. The texture is an important feature for controlling the properties of the ARB-processed sheets, because the ARB process basically fabricates sheet materials. There is limited information, however, as to the texture of ARB-processed sheets.[3,5]

HYOUNG WOOK KIM, Senior Researcher, and SUK BONG KANG, Principal Researcher, are with the Department of Materials Technology, Korea Institute of Machinery and Materials, Changwon, 641-010, Korea. Contact e-mail: hwkim@kmail.kimm.re.kr. NOBUHIRO TSUJI, Associate Professor, and YORITOSHI MINAMINO, Professor, are with the Department of Adaptive Machine Systems, Osaka University, Osaka, 565-0871, Japan.

Manuscript submitted July 25, 2005.

The commercial AA8011 alloy is an Al-Fe-Si alloy, which has a wide variety of applications, owing to the possibility of controlling the microstructure and mechanical properties by means of a specific thermomechanical treatment.[26,27] In a conventional cold-rolling process, however, the total reduction in thickness is limited due to the thickness restriction that results when the strain is increased. The limit of the total reduction in conventional rolling is, therefore, about 95 pct (equivalent strain of 4.0). On the other hand, we[11,13,25] have applied very high strains, over 10, to the AA8011 alloy sheet, by means of the ARB at ambient temperature, and have succeeded in producing UFG AA8011 sheets. We have also found a unique mechanical property[25] that has not yet been reported in severely deformed aluminum alloys. That is, the total elongation of the ARB-processed AA8011 sheet increases significantly with increasing strain after a large drop by one ARB cycle ($\varepsilon = 0.8$). Kim *et al.*[25] showed that a large number of second-phase particles normally included in Al-Fe-Si alloys influenced the microstructural evolution such that the mechanical properties changed during the ARB process. However, little is known about the effect of the texture on the unique mechanical property of the ARB-processed AA8011 sheets.

Additionally, in the rolling process, the strain mode and texture are different with a through-thickness location, especially in the case of a high reduction rate per pass and high-friction conditions between the roll and the rolled sheets, as in the ARB process. The ARB process also leads to accumulated sheets, so that the ARB-processed materials contain a lot of interfacial layers parallel to the sheet surface. The texture of the ARB-processed sheet has more complex features than that of conventionally rolled sheets.[28] In a previous article,[28] we reported about the macrotextural changes that occur with successive ARB cycles, as seen by X-ray diffraction (XRD) pole-figure analysis; meanwhile, the relationship between the microstructure and the microtexture was not explained in detail.

This study aims to clarify the texture evolution of the AA8011 alloy sheet during the ARB process. In order to consider the effect of second-phase particles on the texture formation, we also prepared a commercial-purity aluminum (AA1100) specimen under the same condition as the AA8011.

II. EXPERIMENTAL PROCEDURES

The materials used in this study are commercial-purity AA8011 and AA1100 alloy sheets, the chemical compositions of which are shown in Table I. Hot-rolled plates, 4.0-mm thick, were accepted. In order to get a homogeneous recrystallized microstructure, the hot-rolled plates were cold rolled to the thickness of 1 mm, then annealed at 400 °C for 1 hour.

For the ARB process, aluminum alloy sheets were cut into dimensions 1.0-mm thick, 30-mm wide, and 300-mm long. The surfaces of the sheets were degreased with an acetone and were wire-brushed, to get good bonding prior to roll bonding. The two sheets were stacked so that the brushed surfaces were in contact and fixed tightly to each other with stainless steel wires. The roll bonding was conducted at ambient temperature under a dry condition without any lubricant; the reduction in thickness per cycle was 50 pct (ε = 0.8/cycle), using a two-high rolling mill. The roll diameter was 175 mm and the roll peripheral speed was about 1 m/min, so that the mean strain rate was 1.43/s. The procedures mentioned here were repeated up to 15 cycles, which corresponded to a 99.99 pct reduction in thickness and a total equivalent strain of 12.0. Table II summarizes the total reduction and equivalent strain acquired by the ARB process.

The microstructure was observed using a polarized optical microscope after etching with Baker's reagent, and the distribution of second-phase particles and the morphology of grains were observed on a JEOL*-5800 scanning electron microscope (SEM), operated at 15 kV, and a HITACHI*-800 transmission electron microscope (TEM), operated at 200 kV. Thin foils for the TEM observation were prepared by twin-jet polishing in a 300-mL HNO_3 + 600-mL CH_3OH solution at 253 K.

*JEOL is a trademark of Japan Electron Optics Ltd., Tokyo.

*HITACHI is a trademark, of Hitachi High Technologies Co., Tokyo.

Table I. Chemical Compositions of the AA8011 and AA1100 Alloy Sheets (Weight Percent)

Materials	Si	Fe	Cu	Mg	Ti	Al
AA8011	0.63	0.72	0.01	0.002	0.01	bal
AA1100	0.17	0.57	0.11	0.001	0.02	bal

The macroscopic texture of the samples was measured by XRD, using Cu K_a radiation. The raw data was corrected with the random-texture component of 99.99 pct Al powder samples. The incomplete pole figures were measured mainly at the center of the sheet thickness, and the texture measurements at the subsurface region, 0.01 mm below the real surface after slight electrochemical polishing, were carried out for some specimens. Quantitative texture analysis by orientation distribution function (ODF) was performed using three incomplete poles ({111}, {002}, and {022}). Microtexture measurements by electron-backscattering-pattern (EBSP) analysis were also performed on a PHILIPS* XL30 field emission gun scanning electron microscope (FEG-SEM) equipped with a TSL-OIM* EBSD analysis system. The EBSP measurements were conducted on the longitudinal sections perpendicular to the transverse direction (TD) of the sheets.

*PHILIPS is a trademark of Philips Electronic Instruments Corp., Mahwah, NJ.

*TSL-OIM is a trademark of Ametek, Inc., PA.

III. RESULTS

A. *Initial Microstructure and Texture*

Figure 1 represents the microstructures of the AA1100 and AA8011 aluminum alloy sheets prior to the ARB process. The initial microstructures of the fully annealed sheets are composed mostly of equiaxed grains with mean grain sizes of 21.7 and 27.5 μm, for the AA8011 and AA1100 alloy sheets, respectively (Figures 1(a) and (c)). In a commercial AA1100 aluminum alloy, it is well known that Al_6Fe or Al_3Fe intermetallic compounds are formed during the solidification and the subsequent annealing process, owing to the solubility limit of Fe in a solid Al,[29,30] but the number of these particles is relatively small. Similarly, as shown in Figure 1(b), a few particles can be observed in the present AA1100 alloy sheet. Meanwhile, the AA8011 alloy sheet has a large number of the second-phase particles, the size of which is smaller than 5 μm, due to the higher content of the Si and Fe elements rather than the AA1100 alloy sheet. In the AA8011 sheet, two kinds of particles can be observed (Figure 1(d)), that is, some particles are gray and the others are white in the SEM micrographs. The composition of each particle was analyzed using a JEOL-8800R electron probe microanalyzer (EPMA), the results of which are shown in Table III. From this result and from several references in the literature,[29,31–33] it was confirmed that the white particles are Si precipitates, the gray ones are α-AlFeSi (Al_8Fe_2Si) intermetallic compounds, and the size of the α-AlFeSi compounds is much larger than that of the Si particles.

Table II. Changes in the Geometry of the Specimens; Total Reduction and Strain during the ARB Process in Which Two Pieces of the 1-mm-Thick Sheets are Roll Bonded by a 50 Pct Reduction per Cycle

Number of cycles	1	2	4	8	12	15	N
Number of layers	2	4	16	256	4096	32768	2^n
Layer interval (μm)	500	250	62.5	3.91	0.24	0.03	$1000/2^n$
Total reduction (pct)	50	75	93.8	99.6	99.97	99.99	$(1 - 1/2^n) \times 100$
Equivalent strain	0.8	1.6	3.2	6.4	9.6	12	$\left(2 \ln 2/\sqrt{3}\right)n = 0.8n$

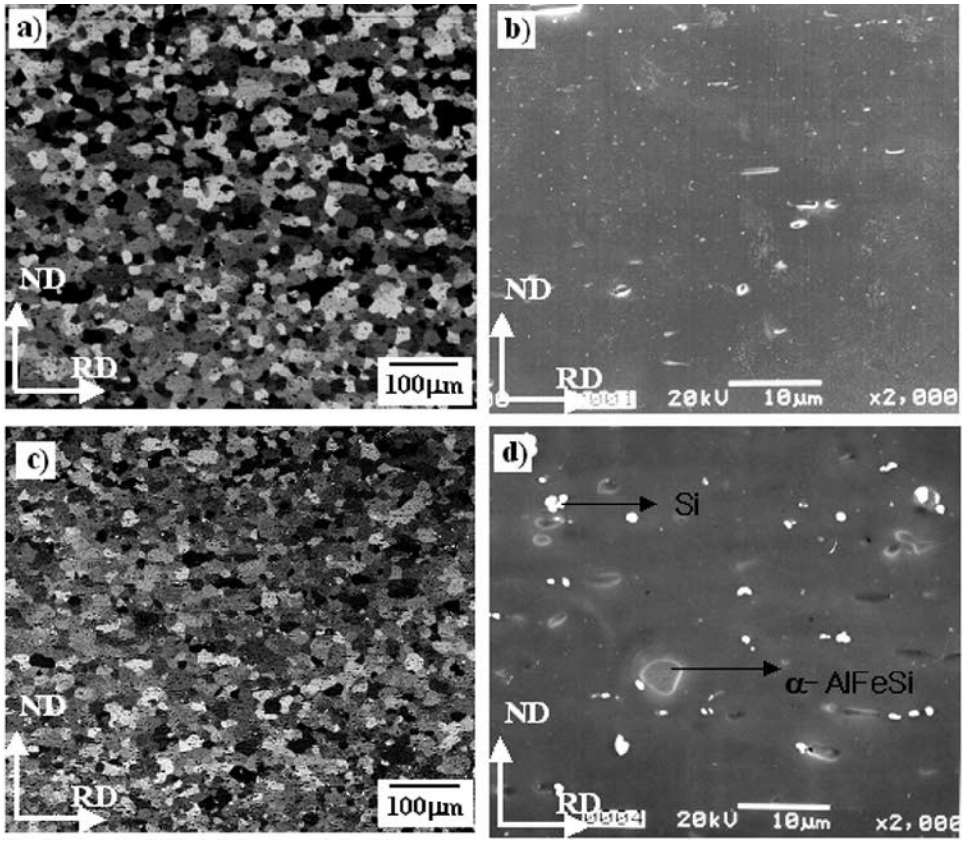

Fig. 1—Microstructures of the AA1100 sheet and the AA8011 sheet before the ARB process. Observed from the TD: (*a*) AA1100 from an optical micrograph, (*b*) AA1100 from a SEM micrograph, (*c*) AA8011 from an optical micrograph, and (*d*) AA8011 from a SEM micrograph.

Table III. The Compositions of Two Kinds of Particles Analyzed by EPMA in the AA8011 Sheets (At. Pct)

White Particle				Gray Particle			
Average Size of Particles (μm)	Al	Fe	Si	Average Size of Particles (μm)	Al	Fe	Si
1.84	57.78	0.03	42.19	1.87	73.27	16.09	10.65

The initial texture of the AA1100 and AA8011 alloy sheets prior to the ARB process was characterized using X-ray macrotexture analysis. Figures 2(b) and (c) are the $\varphi_2 = 45$-, 65-, and 90-deg sections of the X-ray ODF at the surface and the center, respectively, of the annealed AA1100 sheets. Figures 2(d) and (e) are those of the annealed AA8011 sheets. Typical texture components in an Al alloy sheet are also indicated at the same ODF sections in Figure 2(a). The main texture components of the annealed AA1100 and AA8011 sheets are the recrystallized-texture component of cube {001}<100> and the retained-rolling-texture component of Cu {112}<111>. The intensities of each texture component, however, are slightly different in regard to the through-thickness position as well as the alloy compositions. The recrystallized-texture component of cube {001}<100> is clearer at the sheet center than at the sheet subsurface, which might be related to a predeformed state between the surface and the center of the sheets. The texture intensity of the annealed AA8011 sheet is also weaker than that of the annealed AA1100 sheet. That is presumably caused by particle-stimulated nucleation (PSN) during the annealing, due to a large number of second-phase particles in the AA8011 alloy sheet.[26,33]

B. *Texture Distribution along the Through Thickness*

In a conventional rolling process without lubrication, it is well known that an inhomogeneous texture develops through the sheet thickness,[34,35] which is caused by the shear deformation near the sheet surface, due to great friction between the rolls and the material. The intensity and penetration depth of the shear strain are mainly affected by friction, a rolling temperature,[36] deformation geometry in the rolling process,[37,38] and the materials' properties.[39] In the present ARB process, the roll bonding was carried out in a one-pass large reduction (50 pct) under a no-lubrication condition, so that a significant textural gradient through the thickness can be expected. Additionally, because the roll bonding, cutting, and stacking are repeated in the ARB process, the distribution of texture through the thickness may be complex. At first, in order to characterize the crystallographic texture of the

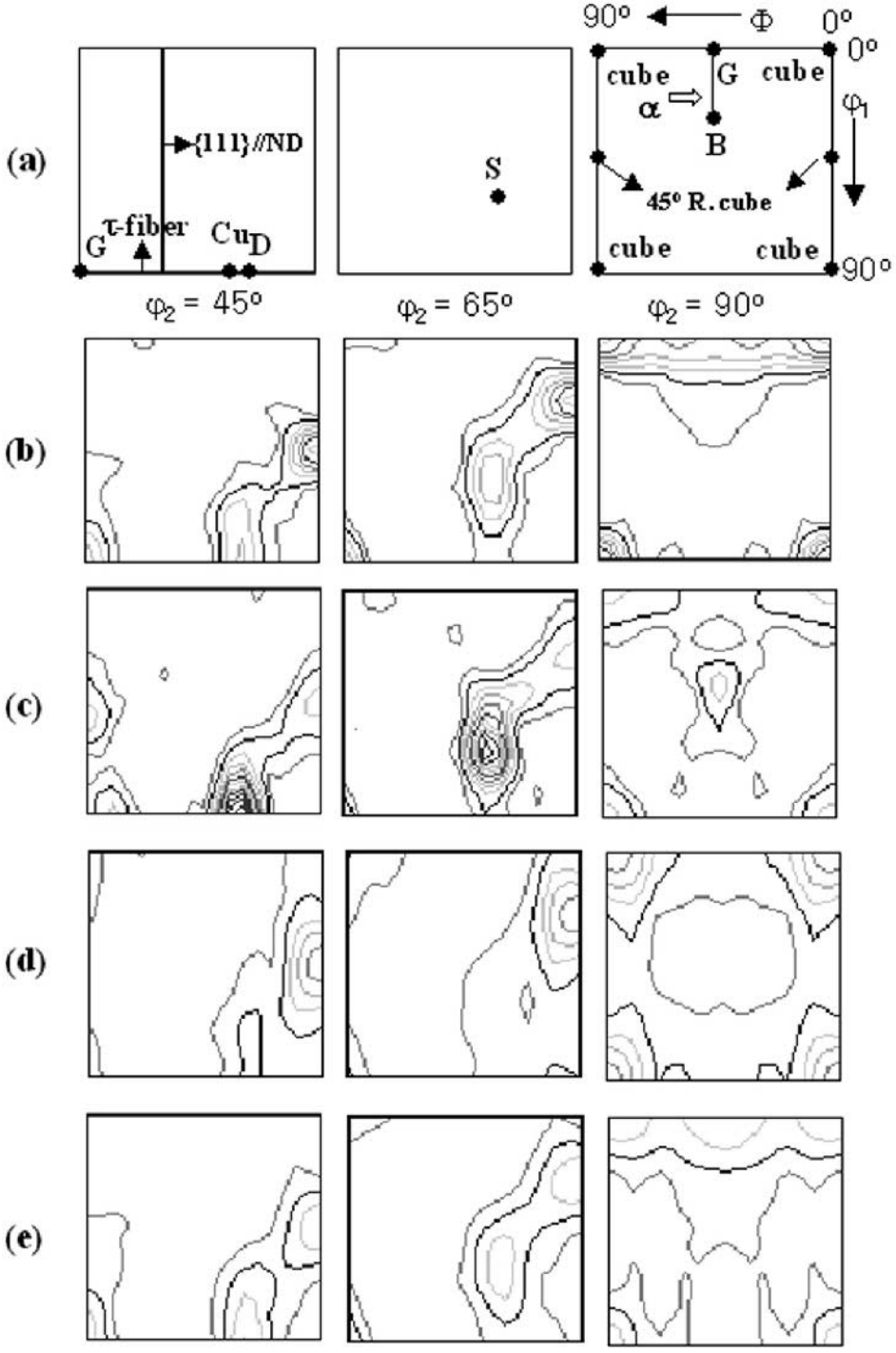

Fig. 2—The φ_2 = 45-, 65-, and 90-deg sections of the X-ray ODFs of the fully annealed AA1100 and AA8011 sheets: (*a*) main ideal texture components on the respective ODF sections; (*b*) AA1100, sheet center; (*c*) AA1100, subsurface; (*d*) AA8011, sheet center; and (*e*) AA8011, subsurface. Contour levels were drawn at, 1, 2, 3, 4, 5, 6, 7, 8, and 9 times random.

ARB-processed aluminum sheet, X-ray pole-figure analysis was carried out at the subsurface and the center of the eight-cycle ARB-processed sheet. Figures 3(b) and (c) are the φ_2 = 45-, 65-, and 90-deg sections of the X-ray ODF at the subsurface and the center, respectively, of the eight-cycle ARB-processed AA1100 alloy sheet. The main texture components at the center consist of a strong rolling-texture component of Cu, {112}<111>, which shifts to a {001}<110> orientation. Meanwhile, the main texture component on the subsurface is composed of the shear-texture component of a 45-deg-rotated cube {001}<110>, along with a minor {111}//ND fiber. The eight-cycle ARB-processed AA8011 sheet shows textural features similar to the AA1100 sheet, except for the intensity. Most of the cube orientation changes to a Cu orientation at the sheet center (Figure 3(d)). At the subsurface, the Cu and cube orientation change to a 45-deg-rotated cube {001}<110> orientation, and a minor {111}//ND fiber (Figure 3(e)). The intensity of the rolling texture at the

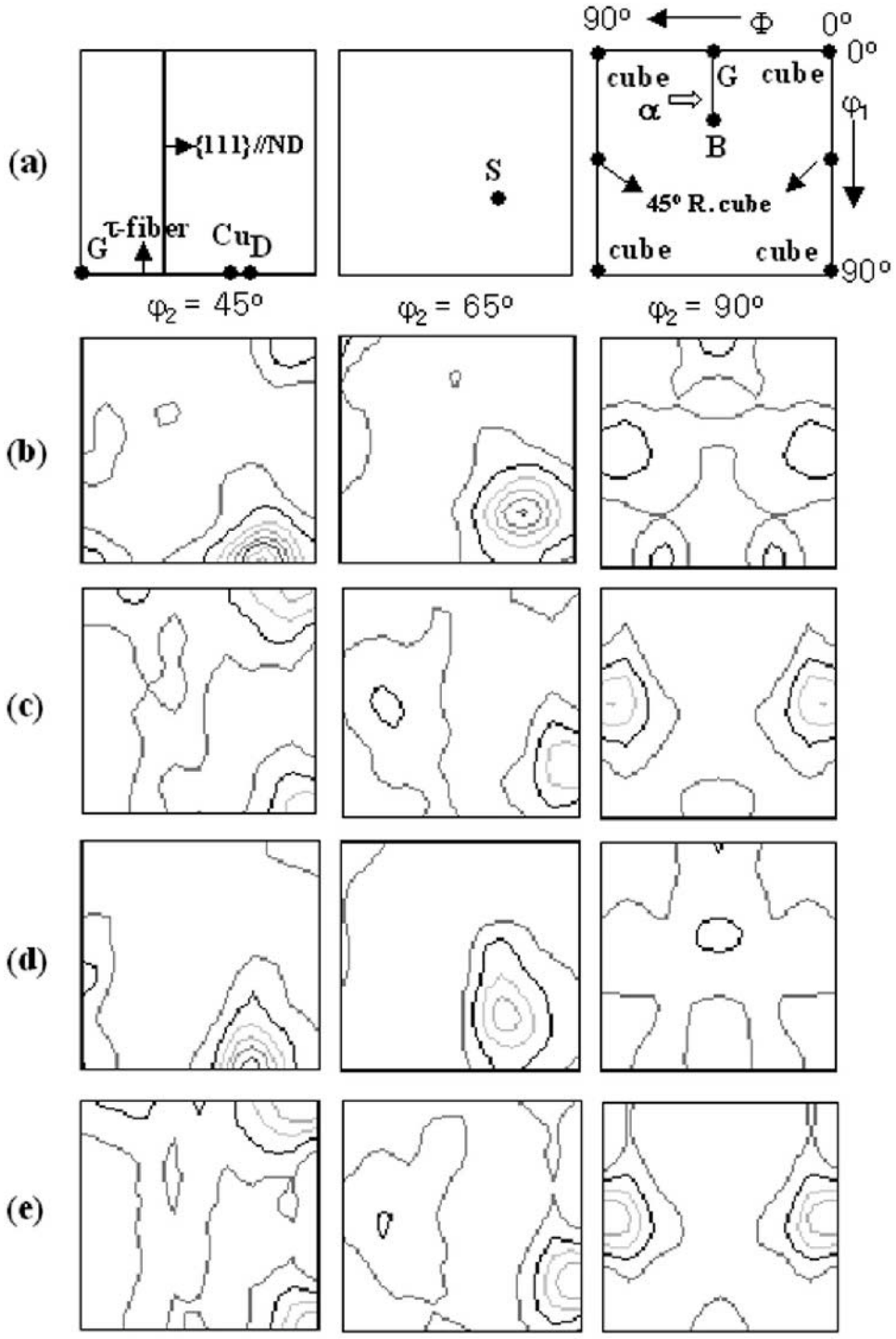

Fig. 3—The φ_2 = 45-, 65-, and 90-deg sections of the X-ray ODFs of the eight-cycle ARB-processed AA1100 and AA8011sheets: (*a*) main ideal texture components on the respective ODF sections; (*b*) AA1100, sheet center; (*c*) AA1100, subsurface; (*d*) AA8011, sheet center; and (*e*) AA8011, subsurface. Contour levels were drawn at, 1, 2, 3, 4, 5, 6, 7, 8, and 9 times random.

center, however, is weaker than that of the conventionally cold-rolled sheets of both materials, at the same strain level. In the ARB process, one of the free surfaces with the strong shear-texture component comes to the sheet center in the next ARB cycle. In the center area, however, there is no shear-texture component. This suggests that the shear texture easily changes to the rolling texture during the next ARB cycle.[34]

As was mentioned earlier, the shear texture at the surface changes to the rolling texture at the center of the sheet thickness during the next ARB cycle. For a more detailed study, the microtexture was investigated by EBSP analysis at the three different thickness locations: at the subsurface (s = 0.9), at the quarter thickness (s = 0.5), and at the sheet center (s = 0.1), in which the s value indicates a relative position

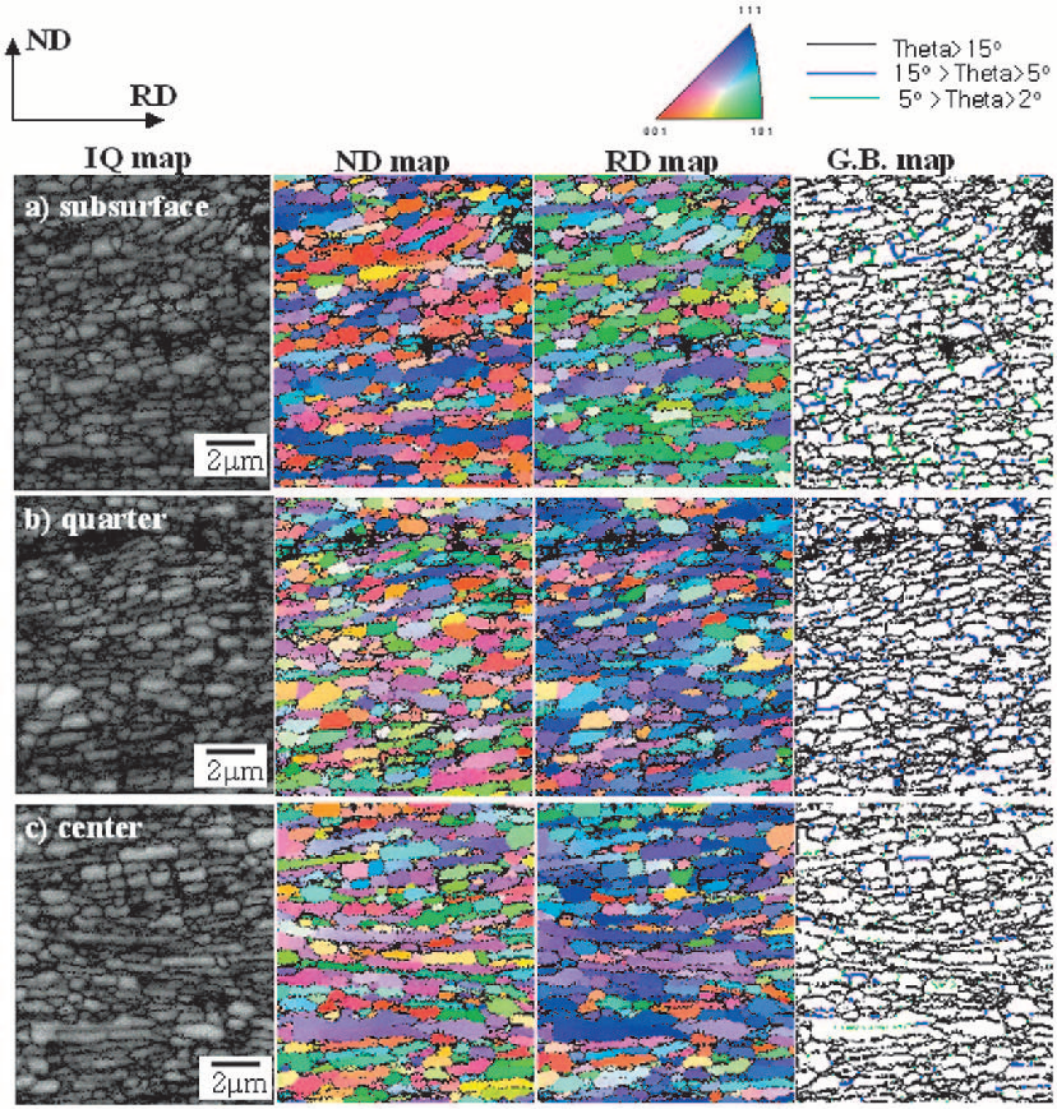

Fig. 4—Orientation maps of the eight-cycle ARB-processed AA8011 sheets observed from the TD at (*a*) subsurface ($s = 0.9$), (*b*) quarter thickness ($s = 0.5$), and (*c*) sheet center ($s = 0.1$). The IQ map is the image quality map; the ND map is the ND-orientation map; the RD map is the RD-orientation map; and the GB map is the grain-boundary-misorientation map.

from the center ($s = 0$) to the surface ($s = 1$). Figure 4 shows the orientation-imaging maps at the three areas of the eight-cycle ARB-processed AA8011 sheet. The EBSD analysis was done on the longitudinal sections. In the figure, the image-quality map describes the quality of the diffraction pattern obtained at a specific point; normal-direction (ND) and rolling-direction (RD) orientation maps indicate the crystallographic orientation of each point parallel to the sample ND and RD, respectively. The correspondence between the colors and the orientations is shown in the stereographic triangle. The misorientation map shows the grain boundaries, along with the misorientation angle between each grain. In the subsurface region ($s = 0.9$, Figure 4(a)), most of the area consists of submicron grains. But, some of the area still has a similar orientation between neighboring grains. In the center region ($s = 0.1$, Figure 4(c)), the shape of the grains is somewhat elongated along the RD. More random orientations are generated to compare with the subsurface region, and most grains have high-angle grain boundaries (HAGB). In the quarter region ($s = 0.5$, Figure 4(b)), the grains have more random orientations, a more equiaxed shape, and a large number of HAGB. Figure 5 shows {111} EBSD pole figures and $\varphi_2 = 45$-, 65-, and 90-deg sections of the ODF obtained from the EBSP measurement at the three different thickness locations. The texture components of the subsurface region ($s = 0.9$) consist of major {001}<110> and minor {111}<110> orientations, as shown in Figure 5(a). At the center ($s = 0.1$), texture components are composed of major Cu {112}<111>, minor Goss {110}<001>, and minor 45-deg-rotated cube {001}<110> orientations (Figure 5(c)). In the ARB process, one of the sheet surfaces comes to the center in the next cycle. Therefore, it can be supposed that the shear texture, composed of {001}<110> and {111}<110> orientations at the surface, changes to the rolling texture composed of Cu {112}<111> and Goss {110}<001> orientations. However, a few {001}<110> orientations still remain. In the quarter region, which was the center in the previous ARB cycle, all shear-texture components disappear and change to Cu and Goss orientations, as shown in Figure 5(b). The orientation relationship between

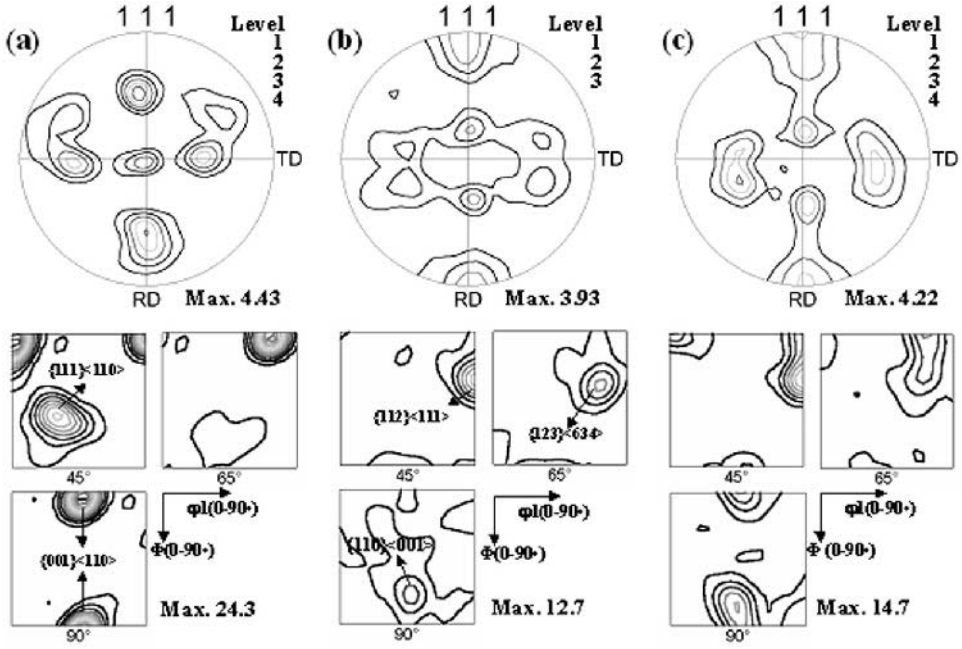

Fig. 5—The {111} pole figures and φ_2 = 45-, 65-, and 90-deg sections of ODFs of the eight-cycle ARB-processed AA8011 sheet: (*a*) subsurface (s = 0.9), (*b*) quarter thickness (s = 0.5), and (*c*) center (s = 0.1). In the ODFs, contour levels were drawn at, 1, 3, 5, 7, 9, 11, 13, 15, 17, 19, 21, 23, and 25 times random.

the Cu {112}<111> and the 45-deg-rotated cube {001}<110> is a 35-deg rotation around the <110> direction. Because the <110> direction in two-texture components is parallel to the TD of the rolling sheets, the 45-deg-rotated cube orientation can be changed to a Cu orientation by the crystal rotation around the TD of the sheet. The {111}<110> orientation at the center can also be rotated to a Goss {110}<001> orientation by a 45-deg rotation around the <001> direction.

For the quantitative study, the orientation intensities ($f(g)$) in each region were calculated; the results are presented in Figure 6. The main texture components of the ARB-processed sheets along the through thickness are the 45-deg-rotated cube {001}<110> and the Cu {112}<111> orientation, which illustrate along τ-fiber. As was mentioned earlier, one of the sheet surfaces comes to the sheet center in the next ARB cycle and then goes up to the quarter thickness in the succeeding cycle. Although the intensity of the {001}<110> orientation is fairly high at the surface, the center and the quarter have a low-fiber intensity, as shown in Figure 6. That is, the {001}<110> shear-texture component changes to a Cu orientation under a plane-strain condition at the center. However, the intensity of the Cu orientation slightly decreases from the center to the quarter-thickness region. During these changes in thickness location and deformation mode, the texture of the sheet changes to a weak-rolling texture. Such textural changes bring about a large misorientation between each grain. Actually, the misorientation angle of the grain boundaries increases at both the center and the quarter-thickness region, as shown in Figure 4.

C. *Texture Evolution during ARB*

As was mentioned earlier, the shear texture at the subsurface changed to the rolling texture at the sheet center during the following the ARB process. These textural changes came from the crystal rotations induced by the plane-strain deformation at the sheet center. Although many surface layers were introduced by the repetition of the ARB process, most shear-texture components at the surface changed to a rolling texture. Therefore, most areas throughout the sheet thickness consisted of a rolling texture, except for the subsurface region. In order to investigate the texture development with successive ARB cycles, the textures at the sheet center of the ARB-processed AA1100 and AA8011 sheets were analyzed by X-ray pole-figure analysis. The intensity of the rolling texture increased with successive ARB cycles in both Al sheets, but the maximum intensities of the texture components showed a different level. For a more quantitative analysis of the texture intensity, the fiber intensity ($f(g)$) was calculated from the X-ray ODF diagrams; the τ-fiber intensities of the two alloy sheets are illustrated in Figure 7. In the case of the ARB-processed AA1100 alloy sheets, the main texture component is Cu {112}<111>. The intensity of the Cu {112}<111> increases continuously with the ARB cycles, and the Φ angle at the peak intensity is shifted toward the {001}<110> orientation and scattered. This behavior has been observed in the materials that have shear bands. In the study of the deformation texture of Cu-oriented pure copper and Al alloys with shear bands, Lücke[33] and Duckham[40] explained that the formation of a shear band was associated with a simple $\pm$ rotation of the original Cu orientation around the TD direction, which led to the shift of the Cu orientation toward the 45-deg-rotated cube orientation {001}<110>.

Meanwhile, in the ARB-processed AA8011 sheets, the maximum intensity of the τ-fiber was obtained at Φ = 27 deg, which coincides with a {4,4,11}<11,11,8> orientation, called the Dillamore orientation. The intensity of the Dillamore orientation increases with increasing strain up to the four-ARB cycle; thereafter, the intensity does not

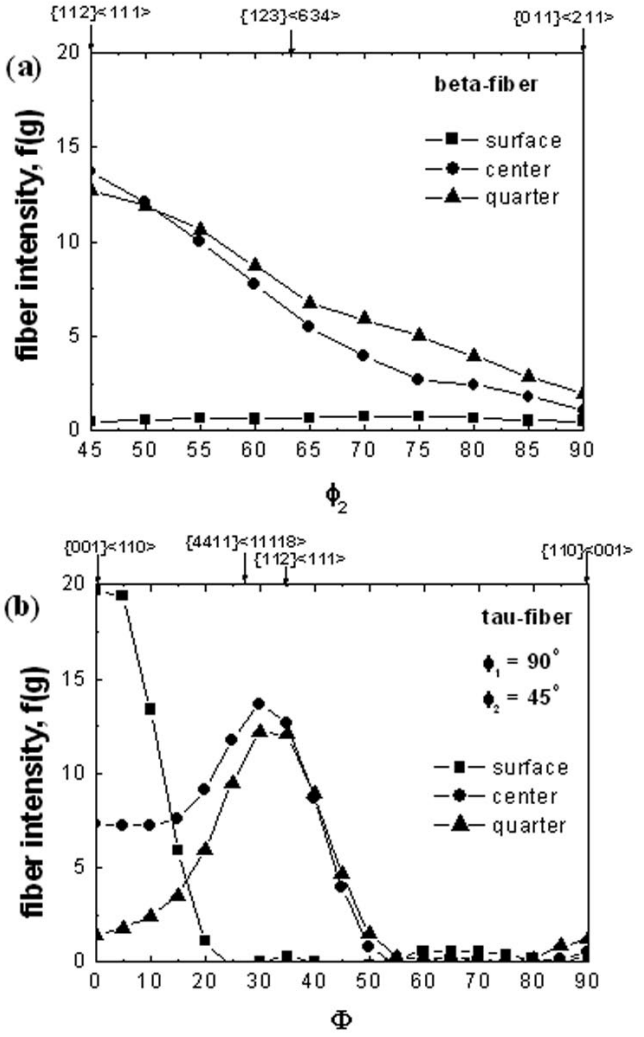

Fig. 6—Orientation densities $f(g)$ along (*a*) β-fiber and (*b*) τ-fiber, at different thickness positions in the eight-cycle ARB-processed AA8011 sheet.

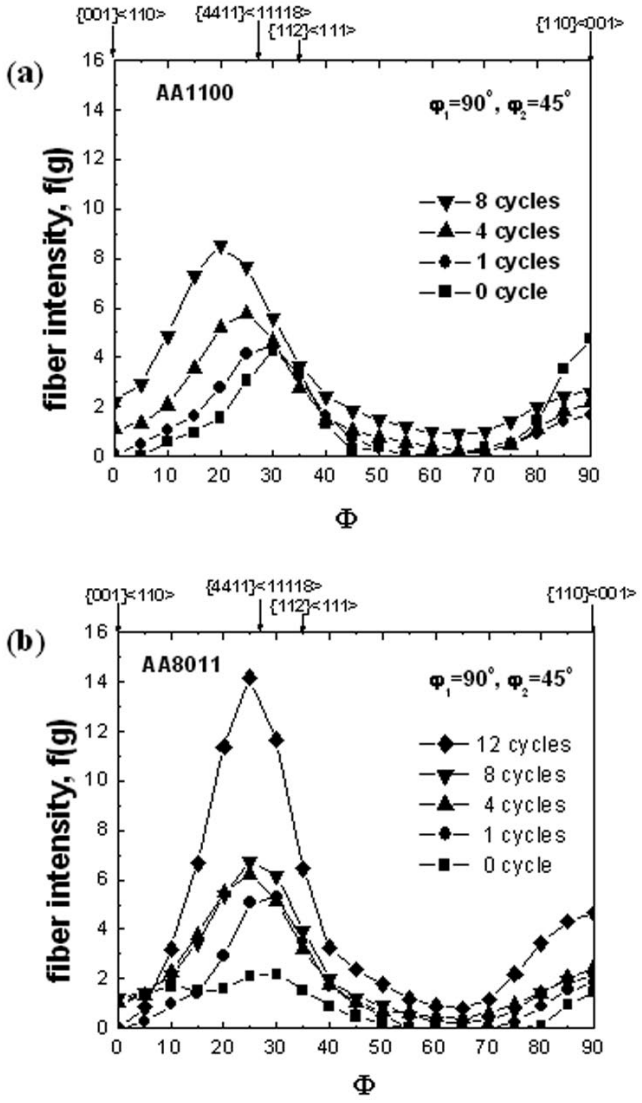

Fig. 7—The X-ray orientation densities $f(g)$ along the τ-fiber at different ARB cycles: (*a*) AA1100 sheet and (*b*) AA8011 sheet.

increase any more. The maximum intensities of texture in the AA8011 alloy sheet are weaker than those in the AA1100 alloy sheet at the same strain level. The AA8011 sheet contained a large number of second-phase particles, which were α-AlFeSi and Si precipitates 1 to 5 μm in size (Figure 1), so that the particles might bring about an inhomogeneous deformation around them, which would result in a weakening of the texture. On the other hand, the Dillamore orientation increases significantly after 12 ARB cycles. This suggests that changes in either the microstructure or the deformation behavior might occur after 12 ARB cycles. The reason for the substantial increase in the deformation texture is discussed in detail in Section IV, as is the microstructure.

The orientation features of individual grains at the sheet center ($s = 0.1$) were investigated by EBSP analysis. Figure 8 is a ND orientation map in the center region ($s = 0.1$), observed from the TD. At the first ARB cycle (Figure 8(a)), the original grains are elongated and subdivided by deformation bands. The subdivided regions have orientations that are different from the original grain. As the ARB cycle increases, UFG structure develops gradually. The ultrafine grain is first formed by shear deformation at the sheet surface. However, grain refinement and crystal rotation seem to be accelerated by the plane-strain deformation at the sheet center, during the following ARB cycles. The orientations of each grain, at four and eight cycles, are quite random, which can be observed by the large differences in brightness between grains, in Figures 8(b) and (c). The randomization of the grain orientation proceeds and the fraction of HAGB increases with the ARB cycles. Meanwhile, after 12 ARB cycles, the differences in grain orientation were small, and the elongated grains with a similar orientation are frequently observed; this is coincident with a substantial increase in the rolling texture after 12 ARB cycles. That is, the development of a special texture such as {4,4,11}<11,11,8> results in a similar orientation between the grains. The β- and τ-fiber intensities were calculated from the EBSP orientation map, and are shown in Figure 9. At the first ARB cycle, the rolling-texture components from Brass {011}<211> to S {123}<634> develops. As the ARB cycle increases, the texture is weakened by the inhomogeneous deformation and the rotation of the shear-texture component. After 12 ARB cycles, the Dillamore orientation increases remarkably. These changes in microtexture

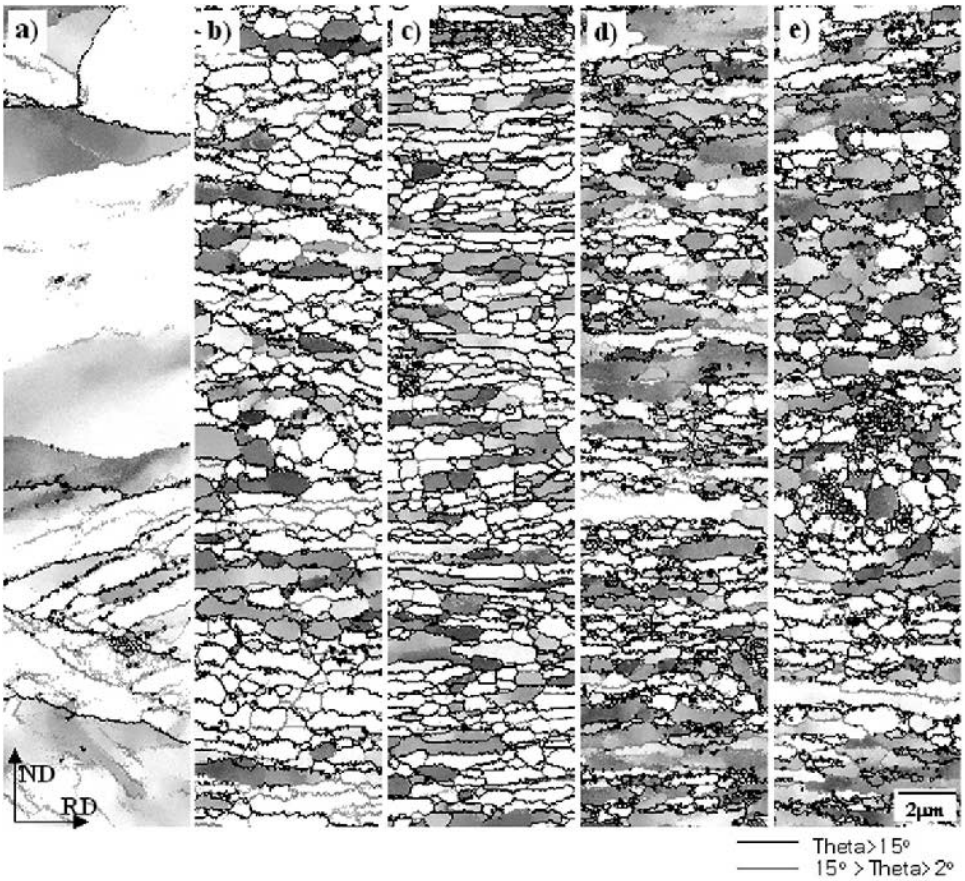

Fig. 8—The ND orientation map at the center region ($s = 0.1$) of the ARB-processed AA8011 sheet: (*a*) 1-cycle, (*b*) 4-cycle, (*c*) 8-cycle, (*d*) 12-cycle, and (*e*) 14-cycle.

intensity correspond well with the X-ray macrotexture results mentioned earlier.

IV. DISCUSSION

In the previous Sections (III-B, III-C), the textural changes of the ARB-processed AA1100 and AA8011 sheets were investigated through the sheet thickness at different ARB cycles. In this section, the textural changes are discussed in detail, along with the microstructural changes that occur during the ARB process.

Figure 10 is the microstructure of the ARB-processed AA1100 and AA8011 sheets observed by a polarized optical microscope, after an electrical etching in Baker's reagent. Although the ARB-processed sheets contained many boned interfaces, they were partially observed only by electrochemical etching. The characteristics of the bonded interface were defined well in a previous article.[12] In the AA1100 sheets, many macroscopic shear bands are shown in Figure 10(a). The numbers of shear bands increase with ARB cycles. It suggests that the shear-band formation results in the shifting and scattering of the Cu orientation, as shown in Figure 7(a). At the eight-ARB-cycle specimen, a large number of edge cracks are generated by the formation of the shear bands. Meanwhile, in the AA8011 sheets, no shear band is observed (Figure 10(b)). The ARB processes could be repeated up to 15 cycles without severe edge cracking. The AA8011 aluminum alloy had a large number of second-phase particles and a high matrix purity, due to the scavenging effect of Fe through the formation of AlFeSi intermetallic particles,[41,42] so that the AA8011 sheets showed good workability during the ARB process, and were free from severe cracks at the sheet edge.[43]

The AA8011 sheets produced by the ARB process showed unique textural changes. Up to eight ARB cycles, the texture was moderate or rather weak. Meanwhile, after 12 cycles, a special texture component, such as the Dillamore orientation, sharply increased. In order to investigate the effects of the microstructure on the textural changes during the ARB process, the textural evolutions were correlated with the microstructures. The ARB-processed AA8011 sheets showed unique microstructural features, due to a large number of second-phase particles and pure matrix. Figure 11 shows the grain morphology around large second-phase particles. Near large second-phase particles, the deformation zone is generated by an inhomogeneous deformation; the matrix grains are bent and rotated around the particle (Figure 11(a)). As the ARB cycles increase, the deformation zone become larger, and some grains show an equiaxed grain morphology (Figure 11(b)). In addition, the pure matrix of the AA8011 alloy may contribute to the weakening of the rolling texture, due to the local enhanced recovery near the particles. The reason for the weak texture of the ARB-processed AA8011 sheets up to the middle-strain range (eight cycles, strain equivalent to 6.4) can be explained by the formation of a deformation zone near large second-phase particles and pure matrix.

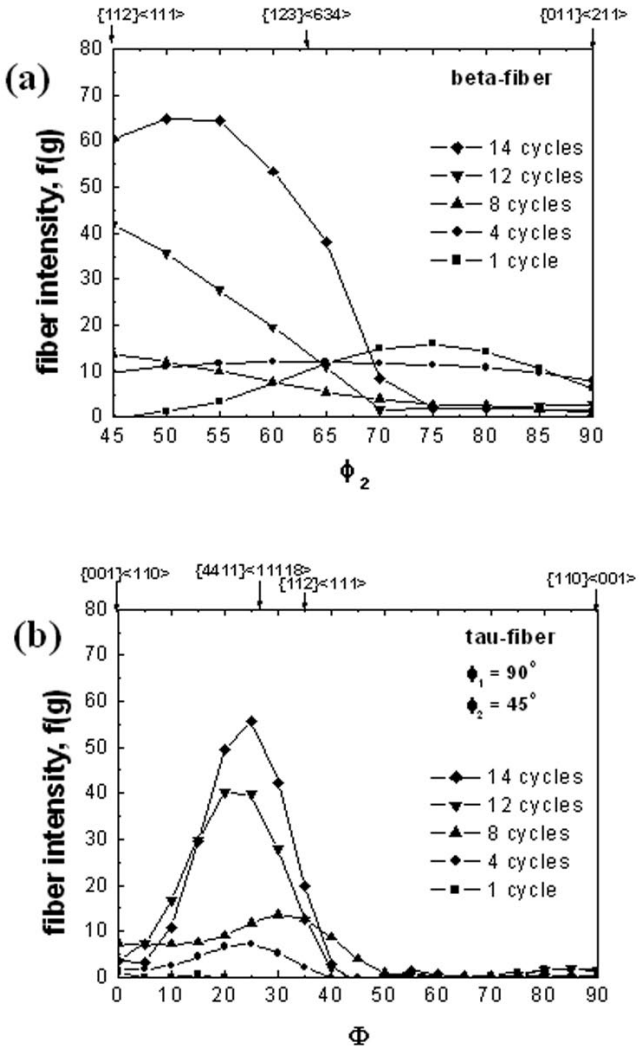

Fig. 9—Orientation densities $f(g)$ along (*a*) β-fiber and (*b*) τ-fiber, at different cycles in the ARB-processed AA8011 alloy sheets.

Lücke and Engler[33] defined the effects of particles on texture evolutions during the rolling process. They remarked that the scattering of the texture was observed in the particle containing aluminum alloys such as the Al-Fe-Si alloy, the Al-Cu-Zr alloy, *etc*. In particular, nonshearable large particles can cause extensive pileups of dislocations, leading to the formation of deformation zones around the particles. Because the initial AA8011 alloy sheet before the ARB contains a large number of second-phase particles, the sizes of which ranged from 0.1 to 5 μm, a large number of deformation zones were introduced in the Al matrix during the ARB process, which weakened the rolling texture.

After 12 ARB cycles, the maximum intensity of the τ-fiber increased with the ARB cycles. After eight ARB cycles, the following major microstructural changes occurred: there was no reduction in the maximum grain size and the fine precipitates formed in the grain interiors, as shown in Figure 12. The microstructural evolution is summarized as follows: at the four-ARB cycle, HAGB were partially formed. The HAGB increased with ARB cycles. After eight cycles, the dislocation density within grains became low, and fine particles precipitated at the grain boundaries and within matrix grains. The number of small particles increased with successive ARB cycles. These results suggested that either the submicron-grain formation or the fine precipitates, or both, had a great effect on strengthening a special texture, such as the Dillamore texture, after 12 ARB cycles.

In a previous article,[25] the microstructural change of the AA8011 aluminum during the ARB process was investigated in detail. It was found that some second-phase particles were broken and dissolved in the Al matrix during severe plastic deformation by the ARB, and then homogeneously precipitated again in grain interiors after 12 ARB cycles. Unfortunately, the exact composition of these particles could not be analyzed, because their size was too small to detect in energy-dispersive X-ray (EDX). Nevertheless, they were expected to be Si precipitates, since the microstructural observations showed that large Si particles were easily broken and dissolved during the ARB. Even when the ARB process was performed at ambient temperature, the temperature of the ARB-processed materials generally increased by an adiabatic heating during the heavy deformation, which was affected by the material as well as by the rolling condition.[19] Therefore, the reprecipitation of Si particles might be stimulated by the deformation heating after 12 ARB cycles, because of the high content of the solute atom in the matrix that results from the subsequent dissolution of the Si particles during the ARB. Meanwhile, in the present study, the AA1100 had a small amount of Si, so that the Si dissolution and reprecipitates were not observed until eight ARB cycles.

Lücke and Engler[33] found that the materials containing small nonshearable particles showed a texture sharpening at high strain, especially the Cu orientation; the texture development was described well by the fully constrained model (Taylor model). It was expected to come from a reduction in the mean free path of dislocations because of the presence of particles. In the ARB-processed AA8011 sheet, the ultrafine grain size and the fine nonshearable particles led to a rather homogeneous Taylor-like deformation (polyslip), which consequently enhanced a special texture formation, such as the stable Dillamore orientation.[44]

It is concluded that the inhomogeneous deformation around the large particles with sizes of 1 to 5 μm resulted in a weak texture in the AA8011 alloy sheets, until eight ARB cycles. In contrast, after eight ARB cycles, the ultrafine grain size (<1 μm) and the fine precipitates (<100 nm) led to a uniform deformation, so that the rolling textures that comprise a Dillamore orientation developed.

V. SUMMARY AND CONCLUSIONS

From the detailed study on the texture evolution of the ARB-processed Al sheets, the formation of the UFG structure was explained well; the explanation took into account the texture distribution through the sheet thickness as well as the textural change during the ARB process. The obtained results are summarized as follows.

1. During the ARB process, the shear texture involving {001}<110> and {111}<110> orientations developed at the sheet surface, due to the shear deformation induced by a large friction between the rolls and the sheet. Meanwhile, at the sheet center, the rolling texture composed of either a Cu texture {112}<111> or Dillamore

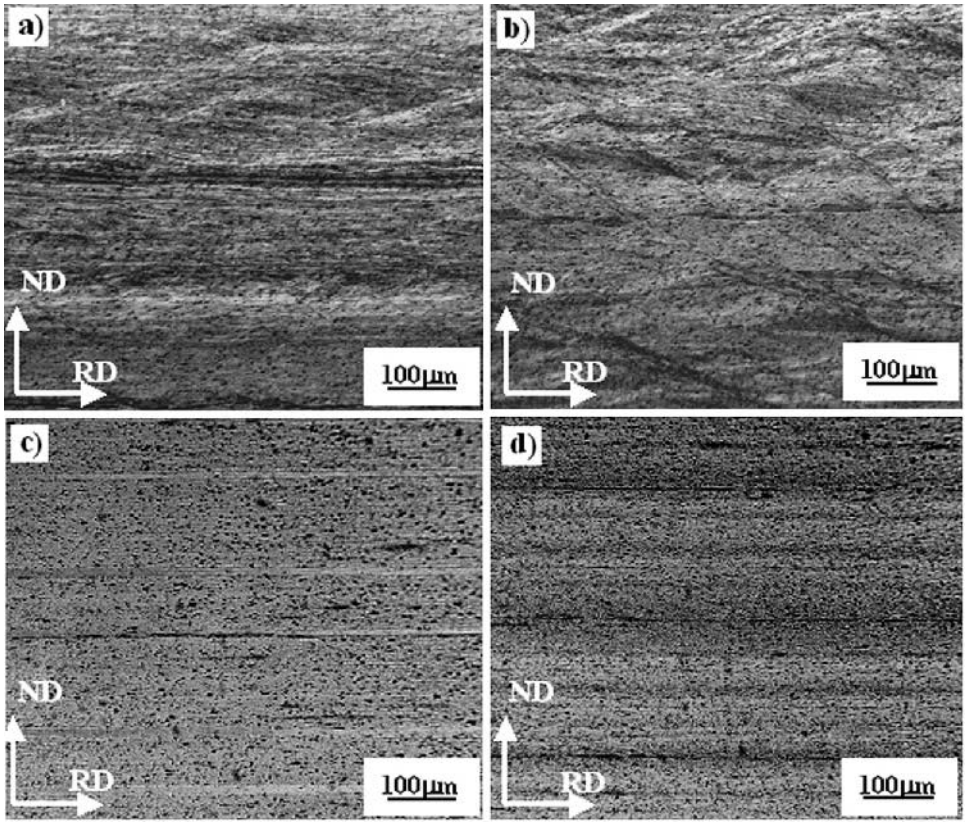

Fig. 10—Polarized optical micrographs of the ARB-processed AA1100 and AA8011 sheets, observed from the TD: (*a*) AA1100, six-cycle; (*b*) AA1100, eight-cycle; (*c*) AA8011, six-cycle; and (*d*) AA8011, 12-cycle.

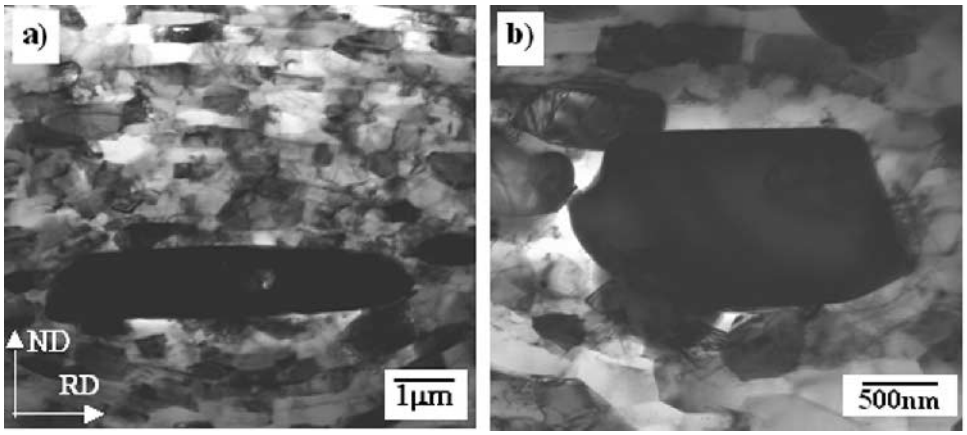

Fig. 11—Grain morphology around large second-phase particles in the AA8011 sheets, with the ARB processed by (*a*) four cycles and (*b*) eight cycles.

{4,4,11}<11,11,8> orientations developed, even though many surface layers are introduced into the sheet by the ARB process.

2. The surface shear texture that developed at the previous ARB cycle was destroyed and changed to the rolling texture at the sheet center by plane-strain deformation. Thus, the final texture in the ARB sheet was mainly composed of Cu {112}<111> or Dillamore {4,4,11}<11,11,8> orientations, except for the sheet surface. Such textural changes during the ARB process contributed to the formation of the high-angle boundaries.
3. As the ARB cycles increased, the intensity of the rolling texture at the sheet center increased until the fourth ARB cycle and, thereafter, the intensity did not increase as much. Also, the maximum intensity of the texture in the AA8011 alloy sheet processed by eight ARB cycles was weaker than that in the ARB-processed AA1100 sheet. This came from the randomization of the texture by the formation of a deformation zone around large, second-phase particles.
4. In the high-strain range (over 9.6, 12 ARB cycles), the intensity of the rolling texture, specifically, a Dillamore orientation, increased remarkably. The main reason for

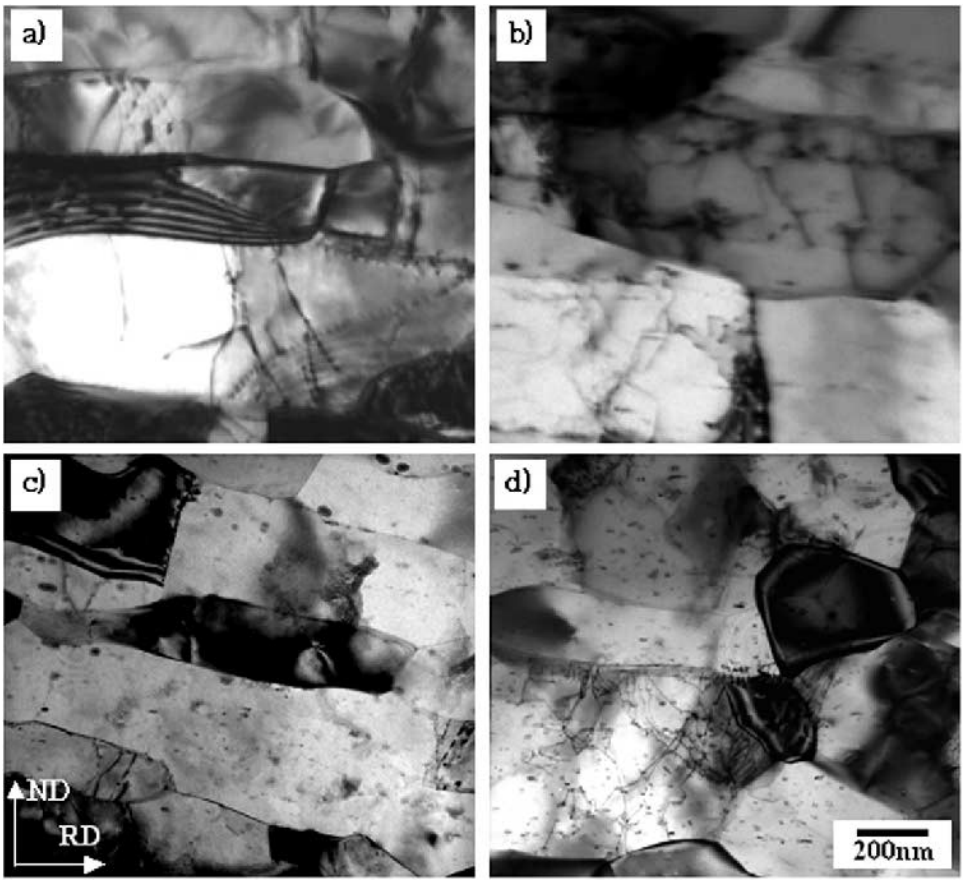

Fig. 12—Precipitation of fine particles in the ARB-processed AA8011 alloy sheets: (*a*) 4-cycle, (*b*) 8-cycle, (*c*) 12-cycle, and (*d*) 14-cycle.

the sharp increase in the Dillamore orientation was the homogenous deformation induced by the reprecipitation of fine Si particles in the grain interiors.

ACKNOWLEDGMENTS

One of the authors (HWK) thanks the Japan Society for the Promotion of Science (JSPS) and the Korea Science and Engineering Foundation (KOSEF), which gave him the chance to participate in cooperative international research at Osaka University.

REFERENCES

1. N. Tsuji, Y. Saito, S.H. Lee, and Y. Minamino: *Adv. Eng. Mater*., 2003, vol. 5, pp. 338-44.
2. Y. Saito, H. Utsunomiya, N. Tsuji, and T. Sakai: *Acta Mater*., 1999, vol. 47, pp. 579-83.
3. Y. Saito, N. Tsuji, H. Utsunomiya, T. Sakai, and R.G. Hong: *Scripta Mater*., 1998, vol. 39, pp. 1221-27.
4. Y. Saito, H. Utsunomiya, N. Tsuji, and T. Sakai: *J. Jpn. Inst. Met*., 1999, vol. 63, pp. 790-95.
5. N. Tsuji, R. Ueji, and Y. Minamino: *Scripta Mater*., 2002, vol. 47, pp. 69-76.
6. N. Tsuji , Y. Saito, H. Utsunomiya, and S. Tanigawa: *Scripta Mater*., 1999, vol. 40, pp. 795-800.
7. N. Tsuji, T. Iwata, M. Sato, S. Fujimoto, and Y. Minamino: *Sci. Technol. Adv. Mater*., 2004, vol. 5, pp. 173-80.
8. N. Tsuji, K. Shiotsuki, and Y. Saito: *Mater. Trans. JIM*, 1999, vol. 40, pp. 765-71.
9. N. Tsuji, K. Shiotsuki, H. Utsunomiya, and Y. Saito: *Mater. Sci. Forum*, 1999, vols. 304–306, pp. 73-78.
10. S.H. Lee, Y. Saito, T. Sakai, H. Utsunomiya, and N. Tsuji: *Proc. 2nd Int. Conf. on Light Materials for Transportation Systems (LiMAT 2001)*, Pohang University of Science and Technology, Busan, Korea, 2001, pp. 635-40.
11. Z.P. Xing, S.B. Kang, and H.W. Kim: *Scripta Mater*., 2001, vol. 45, pp. 597-604.
12. Z.P. Xing, S.B. Kang, and H.W. Kim: *Metall. Mater. Trans. A*, 2002, vol. 33A, pp. 1521-30.
13. S.H. Lee, Y. Saito, T. Sakai, H. Utsunomiya, and N. Tsuji: *Mater. Trans. JIM*, 1999, vol. 40, pp. 1422-28.
14. S.H. Lee, Y. Saito, T. Sakai, H. Utsunomiya, and N. Tsuji: *Mater. Sci. Forum*, 2000, vols. 331–333, pp. 1169-74.
15. T. Sakai, Y. Saito, T. Kanzaki, N. Tamaki, and N. Tsuji: *J. JCBRA*, 2001, vol. 40, pp. 213-17.
16. K. Inoue, N. Tsuji, and Y. Saito: *Proc. Int. Symp. on Ultrafine Grained Steels (ISUGS-2001)*, ISIJ, Fukuoka, Japan, 2001, pp. 126-29.
17. N. Tsuji, R. Ueji, Y. Ito, and Y. Saito: *Proc. 21st Risø Int. Symp. on Materials Science*, Risø National Laboratory, Roskilde, Denmark, 2000, pp. 607-16.
18. X. Huang, N. Tsuji, N. Hansen, and Y. Minamino: *Mater. Sci. Eng. A*, 2003, vol. A340, pp. 265-71.
19. N. Tsuji, T. Toyoda, Y. Minamino, Y. Koizumi, M. Komatsu, and T. Yamane: *Mater. Sci. Eng. A*, 2003, vol. A350, pp. 108-16.
20. X. Huang, N. Tsuji, N. Hansen, and Y. Minamino: *Mater. Sci. Forum*, 2002, vols. 408–412, pp. 715-20.
21. N. Tsuji, T. Murakami, and Y. Saito: *J. Jpn. Inst. Met*., 1999, vol. 63, pp. 243-51.
22. Y. Ito, N. Tsuji, Y. Saito, H. Utsunomiya, and T. Sakai: *J. Jpn. Inst. Met*., 2000, vol. 64, pp. 429-37.
23. N. Tsuji, Y. Ito, H. Nakashima, F. Yoshida, and Y. Minamino: *Mater. Sci. Forum*, 2002, vols. 396–402, pp. 423-28.
24. N. Tsuji, Y. Ito, Y. Saito, and Y. Minamino: *Scripta Mater*., 2002, vol. 47, pp. 893-99.
25. H.W. Kim, S.B. Kang, N. Tsuji, and Y. Minamino: *Acta Mater*., 2005, vol. 53, pp. 1737-49.

26. O. Engler: *Mater. Sci. Forum*, 1998, vols. 273–275, pp. 483-88.
27. R.K. Davis, V. Randle, and G.T. Marshall: *Acta Mater*., 1998, vol. 46, pp. 6021-32.
28. H.W. Kim, S.B. Kang, Z.P. Xing, N. Tsuji, and Y. Minamino: *Mater. Sci. Forum*, 2002, vols. 408–412, pp. 727-32.
29. P. Liu, T. Thorvaldsson, and G.L. Dunlop: *Mater. Sci. Technol*., 1986, vol. 2, pp. 1009-18.
30. R.M.K. Young and T.W. Clyne: *Scripta Mater*. 1981, vol. 15, pp. 1211-16.
31. L.F. Mondolf: *Aluminum Alloys, Structure and Properties*, Butterworth and Co., London, 1976, pp. 534-36.
32. Z.K. Liu and Y.A. Chang: *Metall. Mater. Trans. A*, 1999, vol. 30A, pp. 1081-95.
33. K. Lucke and O. Engler: *Mater. Sci. Technol*., 1990, vol. 6, pp. 1113-30.
34. C.H. Choi, J.W. Kwon, K.H. Oh, and D.N. Lee: *Acta Mater*., 1997, vol. 45, pp. 5119-28.
35. Q. Liu, J. Wert, and N. Hansen: *Acta Mater*., 2000, vol. 48, pp. 4267-79.
36. I.L. Dillamore and W.T. Robers: *Met. Rev*., 1965, vol. 10, pp. 271-380.
37. H.O. Asbeck and H. Mecking: *Mater. Sci. Eng. A*, 1978, vol. A34, pp. 111-19.
38. W. Truszkowski, J. Krol, and B. Major: *Metall.Trans. A*, 1982, vol. 13A, pp. 665-69.
39. B. Major: *Mater. Sci. Technol*., 1992, vol. 8, pp. 510-15.
40. A. Duckham, R.D. Knutsen, and O. Engler: *Acta Mater*., 2001, vol. 49, pp. 2739-49.
41. D.J. Lloyd and D. Kenny: *Acta Metall*. 1980, vol. 28, pp. 639-49.
42. F.J. Humphreys: *Acta Metall*., 1977, vol. 25, pp. 1323-44.
43. J. Hirsch and K. Lucke: *Acta Metall*., 1988, vol. 36, pp. 2863-82.
44. W. Mao: *Mater. Sci. Eng. A*, 1998, vol. A257, pp. 171-77.